nature nanotechnology

ARTICLES

PUBLISHED ONLINE: 20 MARCH 2011 | DOI: 10.1038/NNANO.2011.30

Transforming C_{60} molecules into graphene quantum dots

Jiong Lu[1], Pei Shan Emmeline Yeo[1,2], Chee Kwan Gan[2], Ping Wu[2] and Kian Ping Loh[1]*

The fragmentation of fullerenes using ions, surface collisions or thermal effects is a complex process that typically leads to the formation of small carbon clusters of variable size. Here, we show that geometrically well-defined graphene quantum dots can be synthesized on a ruthenium surface using C_{60} molecules as a precursor. Scanning tunnelling microscopy imaging, supported by density functional theory calculations, suggests that the structures are formed through the ruthenium-catalysed cage-opening of C_{60}. In this process, the strong C_{60}–Ru interaction induces the formation of surface vacancies in the Ru single crystal and a subsequent embedding of C_{60} molecules in the surface. The fragmentation of the embedded molecules at elevated temperatures then produces carbon clusters that undergo diffusion and aggregation to form graphene quantum dots. The equilibrium shape of the graphene can be tailored by optimizing the annealing temperature and the density of the carbon clusters.

Graphene is of great interest because of its unique electronic, thermal and mechanical properties, and it shows promise as a material for use in nanoelectronics[1–7]. Graphene field-effect transistors can be scaled to shorter channel lengths and higher speeds without encountering the adverse short channel effects that restrict the performance of existing devices[8]. Although the vertical scaling of the device can be pushed to the ultimate limit of a single atomic layer in graphene, the problem of lateral scaling is not trivial and requires rather involved top-down lithographical approaches. Currently, top-down lithographical, solution-phase chemical methods and surface-assisted coupling and cyclodehydrogenation of linear polyphenylenes have been applied to produce graphene nanoribbons (GNRs)[4,7,9] and graphene quantum dot (GQD)-based materials[4,6,7,10,11]. Bandgap engineering can be implemented in GNRs and GQDs due to quantum confinement[6,11] and edge effects[9], which is useful for realizing the potential of graphene as a transistor. To date, the majority of solution-phase methods produce irregularly sized and shaped graphene sheets due to the intrinsic randomness of the defect-mediated exfoliation or cutting process of the precursor graphitic flakes. To produce highly regular graphene nanostructures, a fabrication process that is driven by thermodynamics, as in crystal growth, should be more suitable than defect-mediated fragmentation processes.

In principle, graphene and fullerenes are interconvertible. Inspired by the surface-catalysed cyclodehydrogenation of polyaromatic precursors to form fullerenes and the direct transformation of graphene to fullerenes[12,13], we explored the possibility that atomically precise GQDs could be generated from the metal-catalysed cage-opening of C_{60}. The idea is simple: every C_{60} molecule has the same size and shape, so the fragmentation of fullerene, if carried out under well-controlled conditions, should produce uniformly sized GQDs. Carbon nanotubes, onions and graphitic domains have been generated from the optical heating of functionalized fullerenes[14] and the decomposition of fullerenes on metal surfaces[15,16]. However, to date, the opening of the fullerene cage to form GQDs has not been reported. Moreover, the fragmentation mechanism of C_{60} on metal surfaces is not well understood. Depending on the diffusion rate of the C_{60} fragments on a surface, these fragments may combine rapidly on the surface to form large graphitic sheets, or may be confined on surface defects to form featureless clusters. A narrow temperature or coverage window may exist where the interparticle diffusion length favours the growth of GQDs with geometric uniformity. Here, we report a mechanistic approach to the synthesis of a series of atomically defined GQDs by the metal-catalysed cage-opening of C_{60}.

Geometrically well-defined GQDs on Ru(0001)

It is known that a graphitic carbon layer can be derived from the surface-catalysed decomposition of C_{60} adlayers on reactive transition metals. Supplementary Fig. S1 illustrates the transformation of a high coverage of C_{60} ($\Theta > 0.7$ monolayer (ML)) to a single layer of graphene covering a Ru(0001) surface after annealing the sample at 1,200 K for 5 min. Within a coverage range of 0.2 ML $< \Theta <$ 0.7 ML C_{60}, the short diffusion distance between the fragmented molecules favours the aggregation of these carbon clusters, resulting in the growth of larger-sized and irregularly shaped graphene nano-islands (Supplementary Fig. S2). To grow GQDs, the interparticle diffusion length must be sufficiently long (mean distance between C_{60} molecules, 15 ± 3 nm) or the interparticle diffusion velocity must be sufficiently low to limit diffusional aggregation of the decomposed C_{60} fragments. By controlling these factors, GQDs with well-defined geometrical shapes can be assembled from the carbon clusters derived from C_{60}. Figure 1 shows the temperature-dependent generation of GQDs following the annealing of the Ru surface with a low coverage of 0.08 ML C_{60}. Triangular GQDs with a 15 ± 1% yield (apparent lateral size, 2.7 nm) were produced following 1 min annealing at 725 K (Fig. 1a,b). We also observed parallelogram-shaped (2.7×4.2 nm) (Fig. 1c), trapezoid-shaped (2.7×4.8 nm) (Fig. 1d) and hexagon-shaped (10 nm) (Fig. 1f) GQDs, but these have lower yields compared to the smaller hexagonal mushroom-shaped dots (0.9 nm) on the surface (Fig. 1a, inset). Further annealing of the sample at 825 K for 1 min produced 5 nm, perfectly hexagonal GQDs, which have a 30 ± 2% yield (Fig. 1e), while the small-sized (<5 nm) carbon clusters and GQDs disappear. Although some GQDs synthesized here do contain point defects that affect the

[1]Department of Chemistry, National University of Singapore, 3 Science Drive 3, Singapore 117543, [2]Institute of High Performance Computing, 1 Fusionopolis Way, #16-16 Connexis, Singapore 138632. *e-mail: chmlohkp@nus.edu.sg

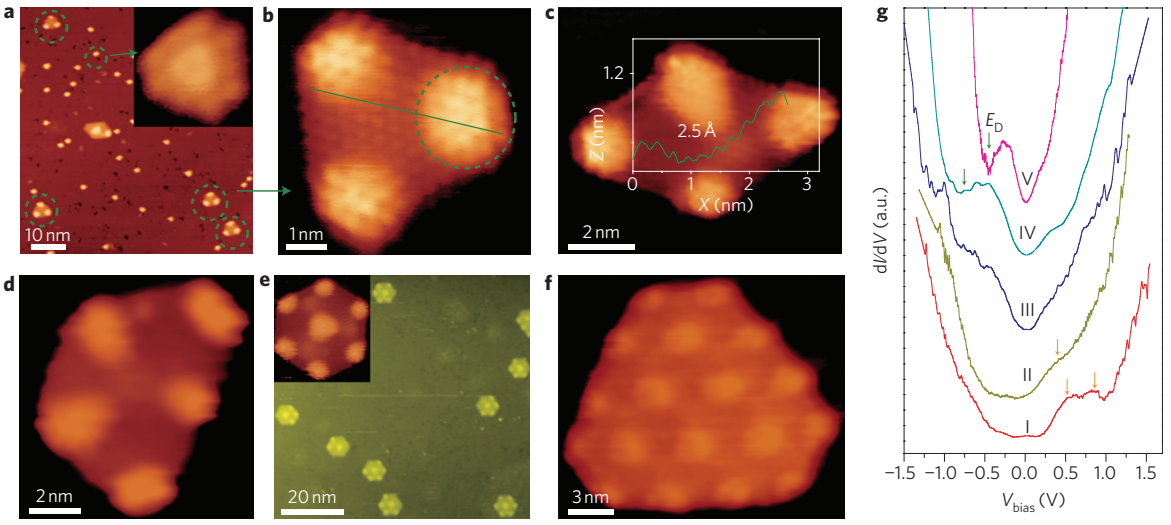

Figure 1 | STM images of GQDs formed by decomposition of 0.08 ML C_{60} on Ru(0001). a, A 0.08 ML C_{60}/Ru sample after annealing at 725 K for 2 min. Inset: magnified view of mushroom-shaped dots. **b**–**d**, Magnified views of triangular (2.7 nm, **b**), parallelogram-shaped (2.7 × 4.2 nm, **c**), trapezoid-shaped (2.7 × 4.8 nm, **d**) GQDs. Inset to **c**: line contour taken along the green line in **b**. **e**,**f**, Hexagon-shaped GQDs (5 nm and 10 nm) obtained after further annealing the sample at 825 K for 2 min. **g**, Representative local STS data for differential conductances dI/dV of the GQDs in **b** (I), **c** (II), **e** (III), **f** (IV) and for giant monolayer graphene on Ru(0001) (V). Tunnelling parameters: $V = 0.5$ V, $I = 0.1$ nA; $V = 0.3$ V, $I = 0.2$ nA for the inset images in **a** and **e**; $V = 0.3$ V, $I = 0.2$ nA (**b**,**c**); $V = 0.3$ V, $I = 0.1$ nA (**d**,**f**).

periodic moiré pattern of graphene on the periphery (Fig. 1e and Fig. 4h), the majority of the GQDs show well-defined geometries.

It is expected that size confinement and the associated edge effects of these two-dimensional nanostructures will give rise to electronic properties that are different from those of bulk materials. Atomically resolved topography reveals that the 2.7 nm GQDs with zigzag edges have 2.5 Å triangular lattice structures ('3-for-6') (inset of Fig. 1c) in both the moiré valley regions (centre area in Fig. 1b) and maxima regions (circled area of Fig. 1b), an arrangement that is unlike that of the large-sized graphene sheets, where the hexagonal honeycomb lattice pattern is present for the moiré maxima regions only[17–19] (Supplementary Fig. S1). The lattice mismatch between graphene and substrate gives rise to the characteristic moiré-type pattern. The vertical buckling of the graphene in the scanning tunnelling microscopy (STM) data[18] gives rise to a 0.8 Å difference in the apparent height between the bright parts and the dark region under a sample bias of 0.3 V. The corrugation between bright and dark regions is also dependent on the sample bias applied, which means the electronic effects in this system result in stronger corrugation than the actual geometric roughness of the graphene layer. The carbon atoms in the valley region interact strongly with the Ru substrate, so the sublattice symmetry of graphene is broken. Only the atoms of one particular sublattice are therefore imaged by STM. In the area where the graphene is buckled and not interacting with the substrate (circled area in Fig. 1b), triangular GQDs exhibit a '3-for-6' image. Several factors could give rise to this, such as the presence of topological frustration[20], which results in the appearance of spin states near the Fermi level that are localized on one particular sublattice of the GQDs (Supplementary Fig. S3), or arising from an edge-induced interference pattern[21].

Measuring the bandgap of the GQDs

The correlation between the electronic properties of GQDs with their atomic structure and lateral size was investigated using spatially resolved scanning tunnelling microscopy (STS). The effect of zigzag and armchair edges on the electronic properties can be excluded, because the GQDs here have uniform zigzag edges. The size-dependent bandgap of the GQDs is shown in Fig. 1g. As indicated in the dI/dV spectra (Fig. 1), the triangular-shaped, parallelogram-shaped and hexagon-shaped (with lateral dimension 5 nm and 10 nm) GQDs exhibit an energy gap of 0.8 eV, 0.6 eV, 0.4 eV and 0.25 eV, respectively (see Supplementary Information for more details). The bandgap of GQDs increases with a reduction in their lateral size, which is analogous to bandgap widening in GNRs with a narrowing of ribbon width[22]. The experimental gap (E_g) versus size (L) relation for GQDs follows the relationship $E_g(\text{eV}) = 1.77 \pm 0.12\ \text{eV nm}/L^{0.9\pm0.1}$ using a least-squares fit (Supplementary Fig. S4), which is a close match to the predicted scaling trend of E_g (eV) = 1.68 eV nm/L from quantum confinement[1,23]. The slight deviation can be explained by the interaction between the GQDs and the Ru(0001) substrate. As the size of the GQDs increases, the discrete energy levels centred at 0.5 eV and 0.9 eV for the 2.7 nm GQDs gradually vanish, and a typical dip at −0.4 eV for epitaxial graphene appears when the size of the GQDs reaches 5 nm, which corresponds to the charge neutral Dirac point of graphene (E_D). At this energy, the linear π bands intersect at a single point in k-space so that charge carriers vanish[19,24,25]. For GQDs larger than 10 nm, a pronounced dip appears at −0.35 eV and the tunnelling conductance increases sharply with energy for both filled and empty states. A negative shift of the Dirac point by 0.35 eV is consistent with a substantial electron doping of the graphene adlayer by the Ru substrate.

Ruthenium-catalysed cage-opening of C_{60}

How do the fullerene cages open and transform into GQDs? A complete fragmentation of a monolayer of C_{60} film would produce five graphene layers if all carbon atoms remain on the surface. However, for a Ru surface adsorbed with monolayer to multilayer C_{60} films, only single-layer graphene was observed on the Ru(0001) surface after annealing at 1,200 K for 5 min (Supplementary Fig. S1). Therefore, it can be inferred that there is substantial gasification of the decomposed carbon fragments. To probe the decomposition process of the fullerene and to examine how the surface-retained fragments can transform into GQDs, we tracked the evolution of a lone C_{60} molecule on Ru(0001) (Fig. 2a). When the substrate covered with 0.03 ML C_{60} was gently heated to 450 K for 10 min, the C_{60} transformed into structures with threefold rotational

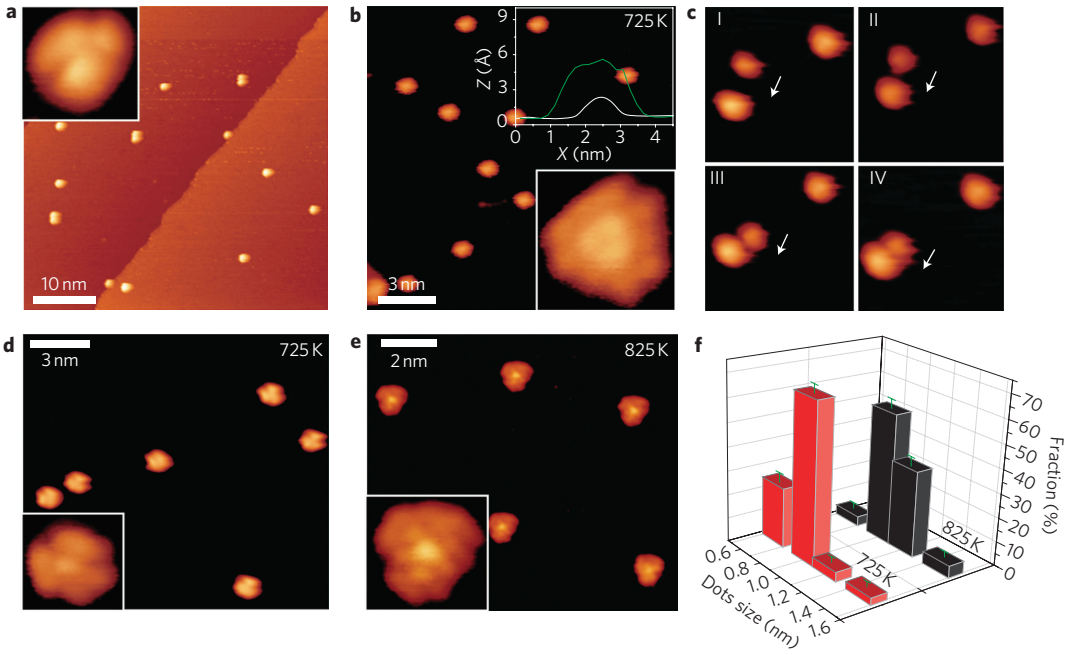

Figure 2 | STM images of the C_{60}-derived clusters after annealing a 0.03 ML film of C_{60} on Ru(0001). a, 0.03 ML C_{60} on Ru (0001). Inset: magnified view of one C_{60} molecule after annealing the sample at 450 K. **b**,**d**,**e**, Bright dots observed after flash annealing at 725 K for 2 min: mushroom-shaped dots (**b**) and flower-shaped dot (**d**); and three flower-shaped dots obtained at 825 K (**e**). Insets (**b**,**d**,**e**): magnified views of these dots. Top inset of **b**: line contour of an individual C_{60} molecule (green curve) and bright dots in **b** (white curve). **c**, Surface diffusion and combination of C_{60}-derived fragments (STM image size, 4.5 × 4.2 nm). **f**, Histogram of dot size distribution at different annealing temperatures: 725 K for 2 min and 825 K for 1 min. Tunnelling parameters: $V = 1.2$ V, $I = 0.08$ nA, $V = 100$ mV, $I = 0.3$ nA for the inset image in **a**; $V = 0.3$ V, $I = 0.2$ nA (**b**); $V = 1.2$ V, $I = 0.1$ nA (**c**); $V = 0.3$ V, $I = 0.25$ nA (**d**); $V = 0.3$ V, $I = 0.16$ nA (**e**).

symmetry (Fig. 2a, inset). One interpretation is that the C_{60} molecule is lying with one six-membered ring parallel to the Ru(0001) substrate, as has been observed for C_{60} molecules on Pt(110) and Cu(111) surfaces[26,27]. After flash annealing for 2 min at 725 K, numerous bright spots that are distinctly different from the starting C_{60} were found on the surface (Fig. 2b,d). The apparent height for these bright spots is 2.7 Å, representing a decrease of 60% from the initial height of 6.5 Å for C_{60} under a similar bias voltage. The lateral size is also significantly reduced (Fig. 2b, inset). Following a detailed investigation, three distinct structures were observed at different annealing temperatures (Fig. 2b,d,e). Annealing to 725 K produced flower-shaped dots with a threefold symmetry (0.7 nm) (Fig. 2d), which constitutes ~23% of the decomposition products (Fig. 2f). Hexagonal mushroom-shaped dots with a lateral width of 0.9 nm were also observed with a 67% yield (Fig. 2b). After annealing at 825 K, the smaller flower-shaped dots appear to have merged into larger ones (1.2 nm) (Fig. 2e). The magnified view of a 1.2 nm dot (Fig. 2e, inset) shows that it originates from the combination of three flower-shaped dots, which are joined at a central protrusion spot. Magnified STM images reveal a triangular lattice pattern for the C_{60}-derived dots rather than the hexagonal-shaped honeycomb lattice pattern of giant graphene. In addition, the atoms at the periphery of the clusters bond strongly to the substrate, resulting in an upward lifting (0.28 ± 0.02 Å in the apparent height for the mushroom-shaped dots) of the centre region relative to the edge, forming a dome-like shape[28]. The strong bonding of peripheral carbon atoms to the substrate suggests that the edges of the clusters are hydrogen-free.

How are the carbon clusters generated from the opening of the C_{60} cage? The STM images in Fig. 3 and Supplementary Fig. S6 provide an insight into this process (the thermal diffusion and sinking of C_{60} molecules are also visualized in a STM-recorded video; Supplementary Movie 1). Annealing the sample to 500–550 K initiates thermal hopping of the C_{60} molecules and dissociation of C_{60} clusters on the terrace. In this temperature range, the diffusion barrier of the isolated C_{60} molecule is overcome and it moves to the on-top adsorption sites on Ru(0001) (Supplementary Table 1). Simultaneously, the Ru atom under the C_{60} hops out to form a vacancy, allowing the C_{60} to sink lower into the surface (with a decreased apparent height of 0.5 ± 0.1 Å; Supplementary Fig. S6). Such an adatom-vacancy mechanism has been observed by Felici and colleagues for C_{60} on Pt(111)[29] and is predicted by Li and colleagues to occur for C_{60} on Ag(111) surface[30]. At the higher annealing temperature of 650 K, embedded C_{60} molecule decomposed to form carbon clusters, as shown in Fig. 3b.

To obtain an atomistic insight into the decomposition mechanism of C_{60} on the Ru surface, the adsorption of a C_{60} molecule on a five-layer Ru(0001) supercell slab was simulated using density functional theory (DFT). The model considers the adsorption of C_{60} on a Ru vacancy site (on-top_vac model) and a non-vacancy site (on-top model) (Supplementary Table 1). The configuration in which the adatom-vacancy mechanism operates is the most energetically favourable. The bond lengths between the C atoms of the bottom hexagon ring and the closest Ru atoms (grey–pink bonds in Fig. 3c) are, on average, 2.0% shorter in the on-top_vac than in the on-top configuration. Likewise, the bond lengths between the second-tier carbon atoms of the C_{60} and the closest Ru atoms (black–pink bonds in Fig. 3d) are on average 2.5% shorter in the on-top_vac configuration. The stronger interaction of the lower hemisphere carbon atoms with the Ru substrate indicates the weakening of certain C–C bonds in the C_{60} molecule. Figure 3d shows the bond lengths of the bottom hemisphere of the optimized C_{60} of the on-top_vac configuration. The C–C long bonds, which are between a hexagon and pentagon ring in C_{60} (labelled in red) in Fig. 3d, have been extended by ~2.6% on average compared to the perfect C_{60}

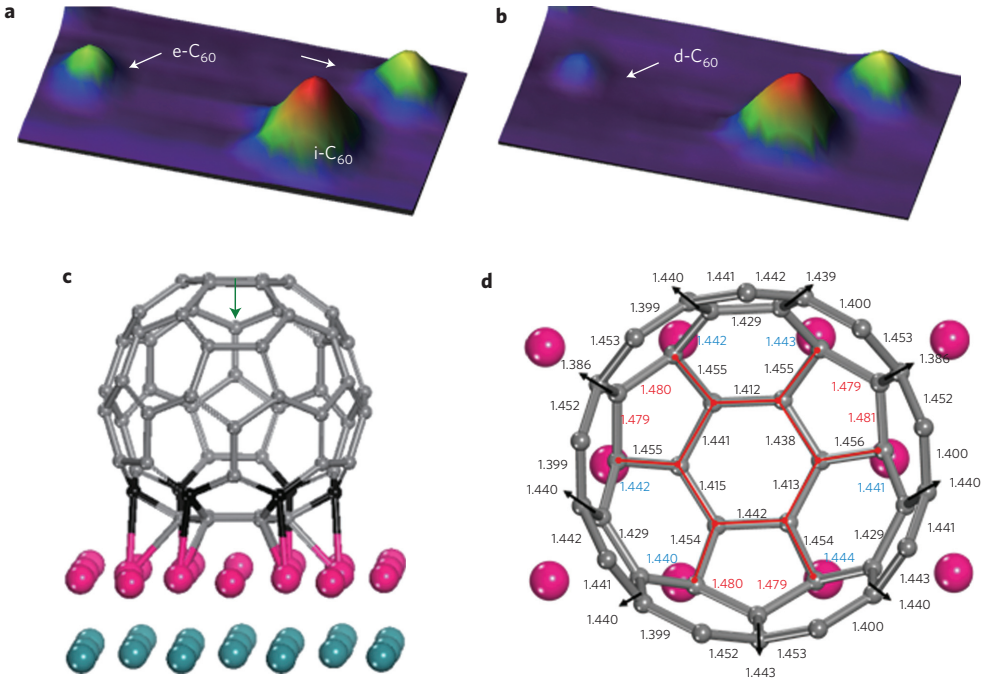

Figure 3 | Three-dimensional STM images of a carbon cluster derived from the decomposition of embedded C_{60} molecules on Ru(0001), and the simulated 'on-top_vac' configuration of a C_{60} molecule on Ru(0001). a, Constant-current image at 600 K (e-C_{60}, embedded C_{60}; i-C_{60}, intact C_{60}; image size, 5 × 3 nm^2). **b**, Constant current image at 650 K (d-C_{60}, decomposition of embedded C_{60}; image size, 5 × 3 nm^2). **c**, On-top_vac configuration of the C_{60} molecule. The single-sided arrow indicates the top-down point of view, from which **d** is derived. **d**, C–C bond lengths of the bottom hemisphere of the C_{60} in **c**. The top hemisphere is not shown for clarity.

molecule, and the C–C short bonds between two hexagon rings in C_{60} (labelled in blue) have been lengthened by ~3.0%. Although the calculations were performed at 0 K, we surmise that these lengthened bonds constitute a fault line that can be ruptured by thermal energy. At higher temperatures, sufficient energy can be generated from the resonance of electron–phonon and phonon–molecular vibronic coupling[31] to rupture the fullerene cages into two unsymmetrical hemispheres along the fault line. The surface-retained fragment derived from the bottom hemisphere of the ruptured C_{60} evolves eventually into the observed surface-stabilized flower-shaped and mushroom-shaped clusters on the Ru surface, while the top hemisphere of the C_{60} cage may desorb into the gas phase.

Peculiarity of a C_{60} precursor in the formation of GQDs

One question is whether the GQDs obtained here are unique to the C_{60} precursor. At a fundamental level, the question is whether the diffusional dynamics of the carbon clusters derived from C_{60} is unique for the growth of GQDs, as opposed to growth mediated by adatom carbon diffusion. To answer this question, we compare the carbon nanostructures produced by C_{60} and C_2H_4 (a commonly used precursor in chemical vapour deposition) in the initial stage of graphene growth. A pictorial summary comparing the growth of GQDs from C_{60}-derivied carbon clusters and large-sized graphene islands from C_2H_4 is shown in Fig. 4.

First, at a low dosage of C_2H_4 (<1 Langmuir (L)), nucleation of C adatoms to form carbon clusters was observed to occur primarily at the step edges of the substrate[32]. It is well known that catalytic dehydrogenation is more facile at these sites and the carbon dimer is stabilized by the step geometry[33]. In contrast, the majority of C_{60} molecules were observed to adsorb on the terraces (Fig. 2a). Second, the much higher mobility of carbon adatoms derived from hydrocarbon decomposition, as well as the tendency for smaller carbon species to dissolve in the bulk and segregate[34], makes it difficult to form small GQDs. Instead, large-sized, irregularly shaped graphene islands are obtained by the Ostwald ripening process[32]. In the case of C_{60}-derived clusters, owing to the limited mobility of the clusters and purely surface-mediated growth, each aggregation event is limited to only a few clusters, leading to the formation of GQDs. We cannot preclude that growth of the GQDs arises from 'one-by-one' addition of carbon adatoms from carbon clusters rather than the coalescence of whole clusters, due to the limited temporal resolution of STM.

A lower diffusion coefficient (in the range of 10^{-15} to 10^{-16} cm^2 s^{-1}) for these C_{60}-derived clusters enables our dynamic STM to capture the cluster movement at high temperature (Fig. 2c and Supplementary Fig. S6). The GQDs derived are equilibrium structures with minimized edge free energy[35], exhibiting highly symmetrical threefold and sixfold structures that are stable to 1,000 K. (Fig. 5 and Supplementary Fig. S9). Some non-equilibrium structures such as parallelogram- and trapezoid-shaped GQDs, which were produced in much lower yield, were also observed. It is instructive to see that these non-equilibrium structures transform into equilibrium shapes by the migration and detachment of edge atoms during annealing (Fig. 5). We captured the dynamic reconstruction of the boundary of these structures using STM video (Supplementary Movie 2). The important stages in the fragmentation processes, which follow the trapezoid → parallelogram → triangle sequence, are captured and highlighted by the brown circles in Fig. 5. Once the islands reach their equilibrium shapes, the growth will cease and their shapes are retained on the surface (Fig. 5 and Supplementary Fig. S9) to elevated temperatures.

In conclusion, we have demonstrated the formation of regularly sized graphene quantum dots on Ru(0001) substrate using C_{60}, which acts as a unique precursor compared to C_2H_4. STM imaging provides direct evidence of the Ru-catalysed cage-opening of C_{60} and the assembly of its fragments into surface-stabilized carbon clusters. Owing to the restricted mobility of these clusters, the aggregation event can be more readily size-controlled than with carbon adatoms derived from a hydrocarbon source. On thermally activated diffusion, these clusters coalesced to form

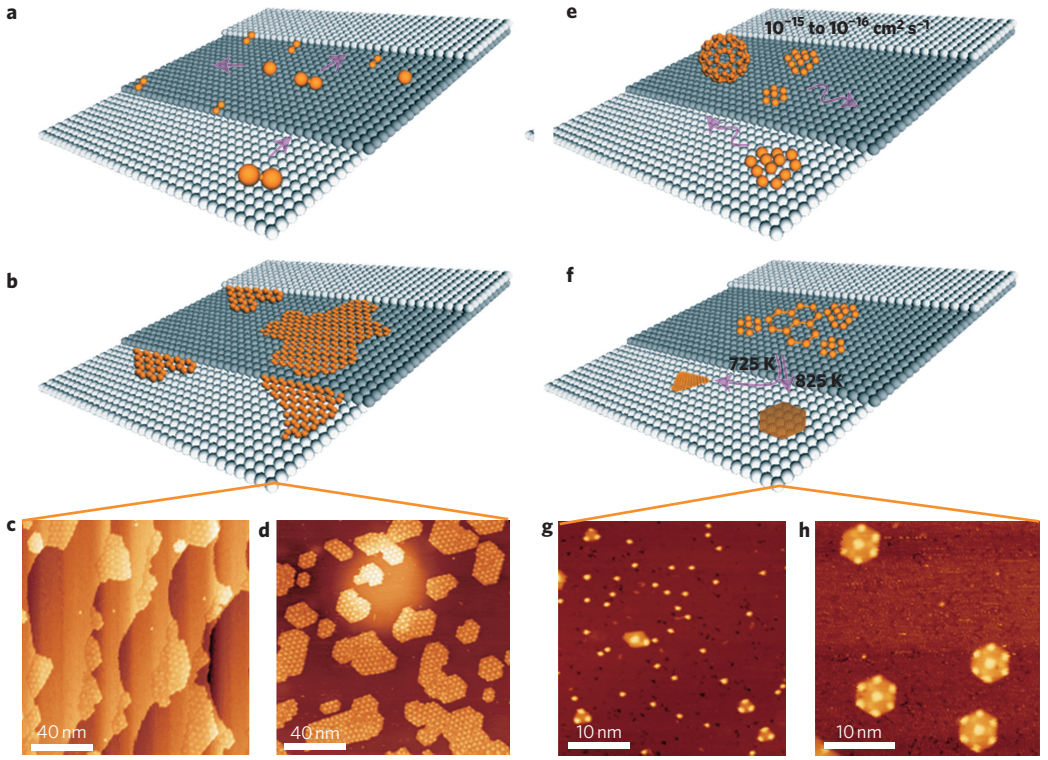

Figure 4 | Comparison of the growth mechanism of graphene nanoislands and quantum dots using C_2H_4 and C_{60}. a–d, Mechanisms using C_2H_4. Highly mobile carbon adatoms from the dehydrogenation of C_2H_4 (**a**). Nucleation of the C adatom occurs at the step edges (at <1 L dose of C_2H_4) (**b**). Large-sized, irregular shaped graphene islands are generated readily (at 1 L $< \Theta <$ 10 L dose of C_2H_4). (1 Langmuir (L) $= 1 \times 10^{-6}$ torr s.) Corresponding STM images for the growth of graphene islands from C_2H_4 (**c**,**d**). **e–h**, Mechanisms using C_{60}. The majority of C_{60} molecules adsorb on the terrace, and these decompose to produce carbon clusters with restricted mobility (**e**). Temperature-dependent growth of GQDs with different equilibrium shape from the aggregation of the surface diffused carbon clusters (**f**). Corresponding STM images for the well-dispersed triangular and hexagonal equilibrium shaped GQDs produced from C_{60}-derived carbon clusters (**g**,**h**). Tunnelling parameters (**c**,**d**, **g**,**h**): $V = 0.5$ V, $I = 1$ nA.

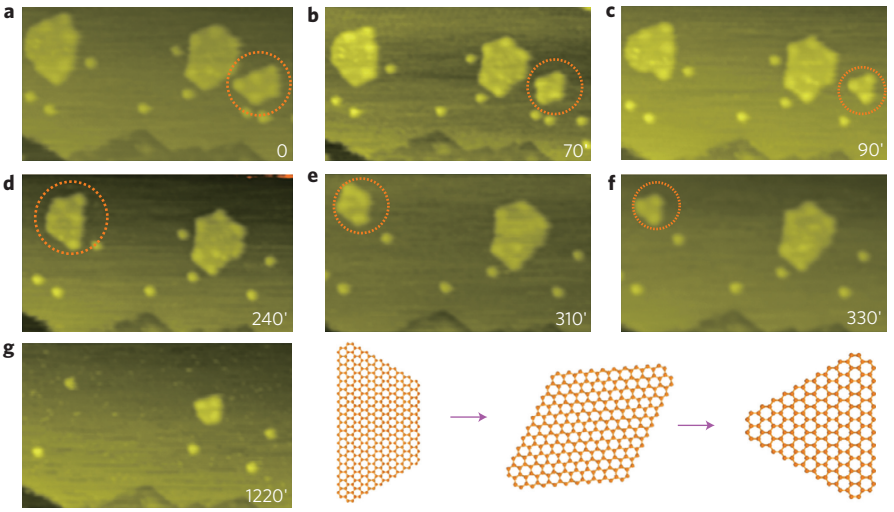

Figure 5 | Series of STM images monitoring the transformation of trapezium-shaped GQDs to triangular-shaped GQDs at 1,000 K. The numbers in the images indicate the time lapse in seconds. Tunnelling parameters (**a**–**g**): $V = 1.4$ V, $I = 0.3$ nA; image size, 25×12 nm^2.

geometrically well-defined GQDs. The adatom-vacancy model relevant to the molecular embedding and fragmentation of C_{60} on the Ru surface may have generic validity for semiconductor or insulator substrates, which can exhibit strong substrate–carbon bonding; the templated growth of GQDs on such surfaces may allow nanoelectronic applications to be developed. Arising from size effects or topological frustration, graphene clusters of different shapes and sizes may also exhibit magnetic properties, and can potentially form building elements for logic gates in ultrafast high-density spintronic devices.

Methods

The experiments were performed in an ultrahigh-vacuum (UHV) chamber at a base pressure of 2×10^{-10} mbar. The STM used was a SPECS STM 150 Aarhus unit.

In addition to STM topographic images, STS data were collected that were an arithmetic average of values measured at 50–70 different points (depending on GQD size) over the surface of the GQDs. The Ru(0001) crystal was depleted of carbon impurities by repeated cycles of argon ion sputtering at room temperature $p(Ar) = 5 \times 10^{-5}$ mbar, 1.0 keV, followed by annealing in an O_2 pressure of 2×10^{-7} mbar at 1,000 K, then flashing to 1,600 K. The vacuum system was also equipped with Knudsen cells (MBE-Komponenten) for the evaporation of C_{60} housed in the preparation chamber. During deposition, the substrate was held at room temperature. The deposition rate of C_{60} was calibrated by counting the surface density of the large-scale STM images with coverage below 1 ML (one layer of fully covered C_{60}).

Spin-polarized simulations based on DFT were conducted using the SIESTA code[36]. The local density approximation for the exchange-correlation functional by Ceperley and Alder was used[37]. We applied Troullier–Martins pseudopotentials[38]. In the case of Ru, relativistic and nonlinear core corrections were added. Double-ζ plus polarization localized basis orbitals were used, with the C (2*s*, 2*p*) and Ru (4*d*, 5*s*) electrons treated as valence. The C_{60} molecule was modelled on a five-layer Ru slab model (Fig. 3) with a $16.08 \times 13.93 \times 26.44$ Å^3 supercell and a $3 \times 3 \times 1$ Monkhorst–Pack sampling scheme. STM image simulations were conducted under the simplifying assumptions of the Tersoff–Hamann theorem[39], which states that STM images may be modelled by calculation of the local density of states (LDOS) around the Fermi level of the surface of interest.

Received 1 December 2010; accepted 15 February 2011; published online 20 March 2011

References

1. Geim, A. K. & Novoselov, K. S. The rise of graphene. *Nature Mater.* **6,** 183–191 (2007).
2. Novoselov, K. S. *et al.* Electric field effect in atomically thin carbon films. *Science* **306,** 666–669 (2004).
3. Choucair, M., Thordarson, P. & Stride, J. A. Gram-scale production of graphene based on solvothermal synthesis and sonication. *Nature Nanotech.* **4,** 30–33 (2009).
4. Li, X. L., Wang, X. R., Zhang, L., Lee, S. W. & Dai, H. J. Chemically derived, ultrasmooth graphene nanoribbon semiconductors. *Science* **319,** 1229–1232 (2008).
5. Li, D., Muller, M. B., Gilje, S., Kaner, R. B. & Wallace, G. G. Processable aqueous dispersions of graphene nanosheets. *Nature Nanotech.* **3,** 101–105 (2008).
6. Ponomarenko, L. A. *et al.* Chaotic Dirac billiard in graphene quantum dots. *Science* **320,** 356–358 (2008).
7. Kosynkin, D. V. *et al.* Longitudinal unzipping of carbon nanotubes to form graphene nanoribbons. *Nature* **458,** 872–875 (2009).
8. Schwierz, F. Graphene transistors. *Nature Nanotech.* **5,** 487–496 (2010).
9. Cai, J. M. *et al.* Atomically precise bottom-up fabrication of graphene nanoribbons. *Nature* **466,** 470–473 (2010).
10. Pan, D. Y., Zhang, J. C., Li, Z. & Wu, M. H. Hydrothermal route for cutting graphene sheets into blue-luminescent graphene quantum dots. *Adv. Mater.* **22,** 734–738 (2010).
11. Li, L. S. & Yan, X. Colloidal graphene quantum dots. *J. Phys. Chem. Lett.* **1,** 2572–2576 (2010).
12. Otero, G. *et al.* Fullerenes from aromatic precursors by surface-catalysed cyclodehydrogenation. *Nature* **454,** 865–819 (2008).
13. Chuvilin, A., Kaiser, U., Bichoutskaia, E., Besley, N. A. & Khlobystov, A. N. Direct transformation of graphene to fullerene. *Nature Chem.* **2,** 450–453 (2010).
14. Krishna, V., Stevens, N., Koopman, B. & Moudgil, B. Optical heating and rapid transformation of functionalized fullerenes. *Nature Nanotech.* **5,** 330–334 (2010).
15. Cepek, C., Goldoni, A. & Modesti, S. Chemisorption and fragmentation of C_{60} on Pt(111) and Ni(110). *Phys. Rev. B* **53,** 7466–7472 (1996).
16. Swami, N., He, H. & Koel, B. E. Polymerization and decomposition of C_{60} on Pt(111) surfaces. *Phys. Rev. B* **59,** 8283–8291 (1999).
17. Marchini, S., Gunther, S. & Wintterlin, J. Scanning tunneling microscopy of graphene on Ru(0001). *Phys. Rev. B* **76,** 075429 (2007).
18. Wang, B., Bocquet, M. L., Marchini, S., Gunther, S. & Wintterlin, J. Chemical origin of a graphene moire overlayer on Ru(0001). *Phys. Chem. Chem. Phys.* **10,** 3530–3534 (2008).
19. Sutter, E., Acharya, D. P., Sadowski, J. T. & Sutter, P. Scanning tunneling microscopy on epitaxial bilayer graphene on ruthenium (0001). *Appl. Phys. Lett.* **94,** 133101 (2009).
20. Wang, W. L., Yazyev, O. V., Meng, S. & Kaxiras, E. Topological frustration in graphene nanoflakes: magnetic order and spin logic devices. *Phys. Rev. Lett.* **102,** 157201 (2009).
21. Ritter, K. A. & Lyding, J. W. The influence of edge structure on the electronic properties of graphene quantum dots and nanoribbons. *Nature Mater.* **8,** 235–242 (2009).
22. Barone, V., Hod, O. & Scuseria, G. E. Electronic structure and stability of semiconducting graphene nanoribbons. *Nano Lett.* **6,** 2748–2754 (2006).
23. Berger, C. *et al.* Electronic confinement and coherence in patterned epitaxial graphene. *Science* **312,** 1191–1196 (2006).
24. Xu, K., Cao, P. G. & Heath, J. R. Scanning tunneling microscopy characterization of the electrical properties of wrinkles in exfoliated graphene monolayers. *Nano Lett.* **9,** 4446–4451 (2009).
25. Zhang, Y. B. *et al.* Giant phonon-induced conductance in scanning tunnelling spectroscopy of gate-tunable graphene. *Nature Phys.* **4,** 627–630 (2008).
26. Larsson, J. A. *et al.* Orientation of individual C_{60} molecules adsorbed on Cu(111): Low-temperature scanning tunneling microscopy and density functional calculations. *Phys. Rev. B* **77,** 115434 (2008).
27. Casarin, M. *et al.* Strong bonding of single C_{60} molecules to (1×2)-Pt(110): an STM/DFT investigation. *J. Phys. Chem. C* **111,** 9365–9373 (2007).
28. Lacovig, P. *et al.* Growth of dome-shaped carbon nanoislands on Ir(111): the intermediate between carbidic clusters and quasi-free-standing graphene. *Phys. Rev. Lett.* **103,** 166101 (2009).
29. Felici, R. *et al.* X-ray-diffraction characterization of Pt(111) surface nanopatterning induced by C_{60} adsorption. *Nature Mater.* **4,** 688–692 (2005).
30. Li, H. I. *et al.* Surface geometry of C_{60} on Ag(111). *Phys. Rev. Lett.* **103,** 056101 (2009).
31. Schulze, G. *et al.* Resonant electron heating and molecular phonon cooling in single C_{60} junctions. *Phys. Rev. Lett.* **100,** 136801 (2008).
32. Coraux, J. *et al.* Growth of graphene on Ir(111). *New J. Phys.* **11,** 023006 (2009).
33. Chen, H., Zhu, W. G. & Zhang, Z. Y. Contrasting behavior of carbon nucleation in the initial stages of graphene epitaxial growth on stepped metal surfaces. *Phys. Rev. Lett.* **104,** 186101 (2010).
34. Sutter, P. W., Flege, J. I. & Sutter, E. A. Epitaxial graphene on ruthenium. *Nature Mater.* **7,** 406–411 (2008).
35. Mo, Y. W., Swartzentruber, B. S., Kariotis, R., Webb, M. B. & Lagally, M. G. Growth and equilibrium structures in the epitaxy of Si on Si(001). *Phys. Rev. Lett.* **63,** 2393–2396 (1989).
36. Soler, J. M. *et al.* The SIESTA method for ab initio order-*N* materials simulation. *J. Phys. Condens. Matter* **14,** 2745–2779 (2002).
37. Ceperley, D. M. & Alder, B. J. Ground state of the electron gas by a stochastic method. *Phys. Rev. Lett.* **45,** 566–569 (1980).
38. Troullier, N. & Martins, J. L. Efficient pseudopotentials for plane-wave calculations. *Phys. Rev. B* **43,** 1993–2006 (1991).
39. Tersoff, J. & Hamann, D. R. Theory of the scanning tunneling microscope. *Phys. Rev. B* **31,** 805–813 (1985).

Acknowledgements

K.P.L acknowledges funding support from an NRF-CRP grant 'Graphene related materials and devices' (R-143-000-360-281) as well as MOE Tier 2 grant 'Structure and dynamics of molecular self-assembled films' (R-143-000-344-112).

Author contributions

J.L. and K.P.L. conceived and designed the experiments. J.L. performed the STM and STS measurement. P.S.E.Y. carried out theoretical calculations. C.K.G and W.P contributed analysis tools. K.P.L supervised the project. All authors discussed the results and analysed the data.

Additional information

The authors declare no competing financial interests. Supplementary information accompanies this paper at www.nature.com/naturenanotechnology. Reprints and permission information is available online at http://npg.nature.com/reprintsandpermissions/. Correspondence and requests for materials should be addressed to K.P.L.